

Microbial Silicification in Sinters from Two Terrestrial Hot Springs in the Uzon Caldera, Kamchatka, Russia

Jennifer E. Kyle and Paul A. Schroeder

University of Georgia, Department of Geology, Athens, GA, 30602, USA

Juergen Wiegel

University of Georgia, Department of Microbiology, Athens, GA, 30602, USA

Silicification of microbial communities is the most pervasive form of mineralization in two terrestrial hot springs in the Uzon Caldera. X-ray diffraction and electron microscopy reveal a diverse sinter mineral assemblage dominated by opal-A with accessory sulfur, sulfides, alunite group minerals, oxides, and oxyhydroxides. Aluminum laminations (reported for the first time) noted in one deposit may slow opal-A transformational rates enabling mineralized microbial remnants to exist longer in the rock record. Although preservation of microbial forms decreases over time, the collective mineral assemblage and patterning suggests that they are the most persistent lines of evidence of life in the geologic record.

Keywords silicification, bacteria, Kamchatka, Uzon, hot springs

INTRODUCTION

Terrestrial hot springs are active sites of siliceous sinter formation throughout the world (Braunstein and Lowe 2001; Cady and Farmer 1996; Konhauser et al. 2001, 2004; Mountain et al. 2003; Rodgers et al. 2004; Phoenix et al. 2006; Kyle et al. 2007). Given the extreme environmental settings in which sinters form (terrestrial hydrothermal areas) sinters have attracted attention of the scientists because it is thought they form in conditions similar to those of early Earth (Konhauser et al. 2001; Russell et al. 2005). The search for evidence of life in early Earth rocks (Walsh and Lowe 1983; Walsh 1992; Rosing 1999; Altermann 2001; Westall et al. 2001; Schopf et al. 2002; Knoll 2003) as well as on other planets (Romanek et al. 1994; McKay et al. 1996; Russell et al. 2005) and moons, has led researchers to study modern sinters as they contain active sites of microbial activity that: (1) rapidly mineralize both live and remnants of recently lysed cells; (2) appear to exhibit a preservation bias towards microorganisms with thick sheaths; and (3) bind metallic ions

to cell surfaces, which facilitates silicification (Konhauser et al. 2003) and enhances the preservation of original morphologies of mineralized organisms (Ferris et al. 1988).

The goal of this study is to characterize the mineral assemblage and the silicification of microorganisms in sinters and associated mats from two hot springs in the Uzon Caldera, Kamchatka, Russia. Microbial identification in the Uzon using molecular and culturing methods is undergoing investigation (e.g., Bonch-Osmolovskaya et al. 1999; Prokofeva et al. 2005; Slepova et al. 2006; Zhang et al. 2006; Zhao et al. 2006) however it is beyond the scope of this study. The intent herein is to identify minerals, examine microbial morphotypes, both living and mineralized, and characterize the spatial relationships between microbial forms and mineralized zones. These silica microbe-mineral relationship provides a framework for insights into other chemical reaction pathways that lead to the formation of phases from mineral groups such as the phyllosilicates, khandites, sulfides, sulfates, and hydroxides.

Geology of the Uzon

The Uzon Caldera is approximately 7×10 km in dimension and is located within the Eastern Volcanic Zone of the Kamchatka Peninsula, about 180 km north of the capital city Petropavlovsk-Kamchatsky and 25 km inland from the Pacific Ocean (Figure 1a, 1b). Pre-caldera volcanism occurred during the mid Pleistocene, 225–370 thousand years ago (kya) and was dominated by basaltic and minor andesitic lava flows and tuff generation (Karpov 1995). During the mid-Upper Pleistocene (175 kya and 225 kya) a series of explosive eruptions produced felsic ignimbrite sheets associated with the Uzon Caldera. Post-caldera activity consisted of the formation of a large lake basin that persisted since 50 to 70 kya. A dacitic resurgent dome formation event occurred 10 to 12 kya, where felsic tuffs were intruded by dacites. An andesitic maar formed during the early Holocene (Karpov 1995; Karpov and Naboko 1990). Glacial activity has also molded the landscape of the caldera, as ice sheets 100–150 m thick descended the slopes of the caldera walls (Karpov 1995).

Received 6 June 2007; accepted 14 August 2007.

Address correspondence to Jennifer Kyle, current address, University of Toronto, Department of Geology, 22 Russell Street, Toronto, Ontario, M5S 3B1, Canada. E-mail: jennifer.kyle@utoronto.ca

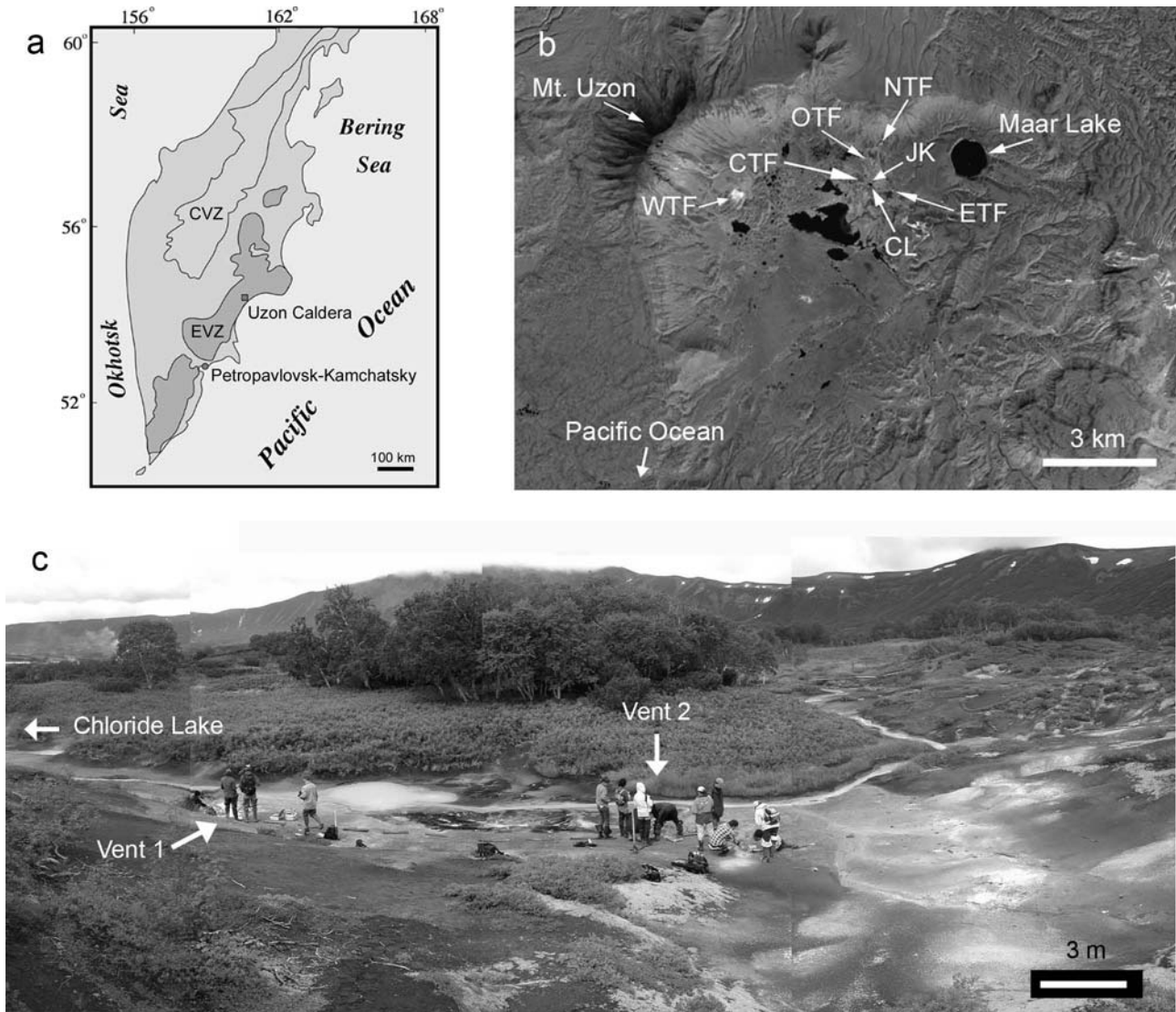


FIG. 1. (a) Map of the Kamchatka Peninsula, Russia showing the Central Volcanic Zone (CVZ) and Eastern Volcanic Zone (EVZ). The Uzon Caldera is located within the EVZ, which is southeast of the CVZ. (b) Satellite photo of the Uzon Caldera (photo from Landsat 7 Enhanced Thematic Mapper Plus (NASA) 15 m resolution). The satellite photo of the Uzon Caldera contains five hydrothermal fields: West Thermal Field (WTF), central sector of Eastern Thermal Field (CTF), Orange Thermal Field (OTF), North Thermal Field (NTF), and eastern sector of Eastern Thermal Field (ETF). Jenn's Pools (JK) are located within the central thermal field along Winding Stream, which flows into Chloride Lake (CL). The large Maar Lake and Mt. Uzon are prominent features of the caldera. (c) Oblique view of Winding Stream (average discharge into Chloride Lake ~ 2 l/s). The stream is mostly fed by Jenn's Pools outflow. Vent 1 is located 13 m downstream from Vent 2.

The Uzon Caldera contains five main hydrothermal fields: Eastern east sector, Eastern central sector, North, West, and Orange (Figure 1b), which collectively contain hundreds of geothermal features located along a main fault trending WNW and subsidiary faults trending NNE. Deep thermal waters are sodium chloride-rich in composition and constitute the largest active sulfide ore-forming hydrothermal system in the Kurile-Kamchatka region (Karpov and Naboko 1990). Hydrothermal activity is driven by a magma chamber situated 2–10 km below the caldera floor (Karpov 1995). Colluvial deposition from the

caldera walls and alluvial deposits cover most of the geothermal regions.

Field Site

Jenn's Pools are located in the Eastern Central sector Thermal Field (CTF; Figure 1b, c). They were chosen for study because of their abundance of siliceous sinters forming around springs and the visible association of microbial mats. The springs, referred to as Vent 1 and Vent 2 (Figure 2), are comprised of

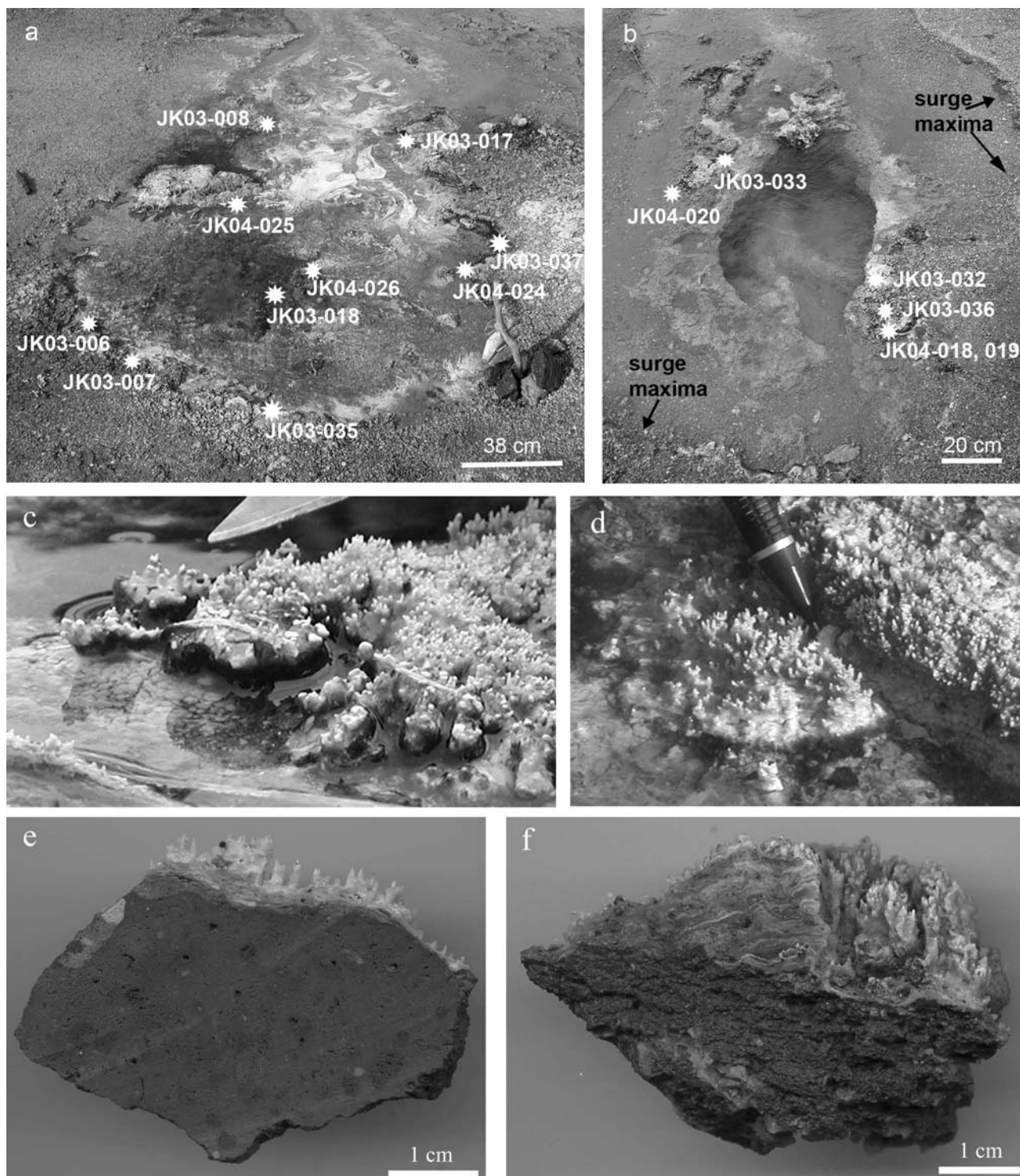


FIG. 2. Photographs of Jenn's Pools comprised of Vent 1 and Vent 2. Sampling sites for Vent 1 (a), and Vent 2 (b) are shown with an asterisk, and are indicated by the sample number. Surge maxima for Vent 2 are shown by the outer rim surrounding the vent (arrows), and surge minimum is confined within the vent. Close up images of sinters collected from the field: Vent 1 (c) and Vent 2 (d). Knife blade and pencil shown for scale. (e) and (f) Cross-sections of the sinter and substrate specimens collected Vents 1 and 2 respectively, for XRD analysis. The sinters comprise the upper millimeter to centimeter of the deposits. Rock underlying the sinters is comprised mostly of dark gray to black and white clays (see figure 6). Samples shown are from Vent 1: (a) JK03-008 and from Vent 2: (b) JK03-032a

TABLE 1
Physiochemical composition of Jenn's Pools. Values are given in ppm unless otherwise noted.

	Vent 1	Vent 2
T (°C)*	83	85
pH*	5.9	5.9
Eh (mV)*	-240	-240
D/H	-111.38 per mil	-106.35 per mil
$\delta_{18}\text{O}$ (SMOW)	-14.51 per mil	-13.66 per mil
Alkalinity (CaCO ₃)	220	160-180
*SO ₄ ²⁻ *	130-188	124-300
PO ₄ ³⁻ *	1.5-1.9	0.35-1.81
NO ₃ ⁻ *	4.0	0.7
NO ₂ ⁻ *	0.019	0.025
DO*	0.3-1.8	1.5-1.9
Total As*	0.1	n.d.
Ag	0.0073	0.0073
Al	0.21	0.18
Au	8.70	5.14
B	4.16	5.09
Ba	0.87	0.82
Be	0.0009	0.0004
Ca	21.64	28.01
Cd	0.0081	0.0059
Ce	0.028	0.015
Co	0.0026	0.0007
Cr	0.012	0.009
Cu	0.035	0.0019
Fe	0.73	0.37
Hg	0.22	n.d.
K	14.77	16.6
La	0.0025	0.00046
Li	105.31	100.25
Mg	5.92	3.81
Mn	0.62	0.61
Mo	0.0084	0.0084
Na	78.71	91.88
Ni	0.0073	0.0045
P	0.21	0.20
Pb	0.069	0.071
Sb	0.27	0.23
Se	0.14	0.16
Si	129.6	138.6
Sr	0.068	0.095
Ti	70.23	103.61
Tl	0.21	0.18
V	0.0086	0.0064
W	0.037	0.18
Y	0.11	0.032
Zn	0.028	0.020

*Values measured *in situ* n.d. = not determined.

two high-temperature outflows, separated by a distance of 13 m. Both discharge into Winding Stream, which flows into Chloride Lake at a discharge rate of about 2 liters per second (Figure 1b, c). Oxygen and hydrogen isotope data (see Table 1) indicate the spring fluids are dominated by meteoric sources (as opposed to juvenile water with magmatic origins). Physiochemical characteristics of each spring are reported in Table 1. Microbial mats, siliceous sinters, and rock substrates (rock upon which sinters are precipitating) were collected in late summer of 2003 and 2004 from the rims of Vent 1 and Vent 2. Seventeen representative sinter samples with attached microbial mats were taken from all sides of Vent 1 and Vent 2 (Figure 2), 11 of which were chemically preserved for electron microscopy as detailed later.

Vent 1 is downstream from Vent 2 and can be hydrologically characterized as a spring with steady discharge and no rim overflow. In contrast, Vent 2 surges at a rate fluctuating between 3 to 17 minutes, with surge maximum overflowing the rim (Figure 2b). The water height change between Vent 2 surges is ~10 cm. Both Vent 1 and Vent 2 sinters form above the air/water interface within the splash zone of the springs. Siliceous sinters form along the rims of the springs, and are composed of spicules (a few millimeters in length) that are directed skyward (Figure 2c, 2d). Thin (<5 mm thick) green microbial mats are commonly found on the sides and between the spicules. Other microbial mat structures were also noted, especially within the outflow channel of Vent 1, which included white filamentous streamers dominated by *Aquaficales* sp. (Lalonde et al. 2005).

METHODS AND MATERIALS

Bulk mineral analysis of the sinters and underlying rock was conducted using X-ray diffraction (XRD; Scintag XDS2000) with a Co K α radiation source. Samples were cut from cross-sectioned pieces (Figures 2e, 2f) and then ground into a fine powder (<20 μm) using a mortar and pestle. Powders were mounted onto a zero-background quartz plate using acetone slurry for random orientation (Hurst et al. 1997). Initial scans were conducted using 2 $^\circ$ /4 $^\circ$ scattering slits, 0.5 $^\circ$ /0.2 $^\circ$ receiving slits, and a 0.6 second counting time at a continuous scanning rate of 2.0 $^\circ$ /min. Low signal-to-noise ratios for sinter material required data collection parameters to include a step count of 0.01 $^\circ$ and 10-15 second count times.

Electron microprobe analysis was conducted using a JEOL 8600 Superprobe with an accelerating voltage of 15 kV. Carbon coated thin sections were analyzed for their elemental composition using energy dispersive spectroscopy (EDS) or wavelength dispersive spectroscopy (WDS). Si, Al, Fe, and S were spatially mapped using WDS to determine distributions within the sinters.

Eleven samples collected from Vent 1 and Vent 2 (Figure 2a, 2b) were chemically preserved to obtain morphological characteristics and microorganisms-mineral relationships. Features were imaged using a Leo[®] Field Emission 982 Scanning

Electron Microscope (SEM). Beam currents operated at 5 kV for secondary electron imaging and up to 25 kV for backscatter electron imaging. EDS analysis was conducted on mineral coatings on microbial cells, microbe-like structures, and crystal faces.

Samples from 2003 (JK03) and 2004 (JK04) were prepared using different fixative protocols because a new technique became available (Bennett and Engel 2004). 2003 samples were submerged in 2% glutaraldehyde and stored at ambient room temperatures until returned to the lab. (i.e., maximum preservative period was 2 weeks in glutaraldehyde). Samples were transferred into phosphate-buffered saline (PBS) for three 10-minute washes and stored at 4°C overnight in osmium buffer solution. After rinsing 3 times with distilled water, samples were subject to a 30-minute stepwise dehydration series using ethanol. Critical point dried samples were mounted onto aluminum stubs and carbon coated for SEM and EDS analysis.

The 2004 samples followed the fixation protocol of Bennett and Engel (2004). Samples were immediately washed 3 times at 10-minute intervals in 0.05 M Cacodylate buffer and then transferred into a mixture of 2% glutaraldehyde, 50 mM lysine, and 0.05 M Cacodylate for 90 minutes. Samples were then stored in the glutaraldehyde-Cacodylate buffer until their return to the lab (approximately 2 weeks). Samples were transferred into osmium buffer solution and stored at 4°C overnight. The same ethanol dehydration series as above was used (20 minute intervals) and then chemically dried in hexamethyldisilazane (HMDS) twice at 20-minute intervals. Samples were left to air-dry overnight, mounted on aluminum stubs, and carbon coated for viewing on the SEM.

Transmission electron microscopy (TEM) sample preparation followed the same fixing protocols. Additional fixation proceeded by infiltration with propylene oxide for 45 minutes. Samples were transferred to a 2:1 propylene oxide to Epon resin mixture, then a 1:2 mixture, then twice in 100% resin at 1.25 hours intervals. After a third transfer to resin overnight, samples were cured at 60°C until the resin hardened. Samples were sectioned using a diamond ultra-microtome and then mounted on Formvar coated copper grids. Samples were examined by TEM before and after staining with uranyl acetate and lead citrate. These stains normally create electron dense artifacts to enhance certain cellular membranes. The comparison helps to recognize naturally occurring electron dense nanoparticles within the samples. Samples were analyzed using a Philips 420 analytical TEM, employing EDS and selected area electron diffraction (SAED). A Philips CM300 TEM was used for electron energy loss spectroscopy.

Water samples from each spring were analyzed *in situ* using HACH kits, pH/Eh meters, pH paper, and digital thermometers. Duplicate 50 ml samples were filtered using a 0.2 µm filter and returned to the lab for analysis. One duplicate sample was acidified on site with ~0.5 ml 5N sulfuric acid to avoid precipitation of some elements (e.g., Fe). After blank correction dissolved elemental concentrations were measured using Induction Coupled Plasma Mass Spectrometry (ICP-MS) where an argon plasma torch ionizes the sample into elemental species and a quadrupole mass spectrometer separates the charged species by

mass to charge ratios and detects elemental species and concentrations (Tanner et al. 2000). The second duplicate was analyzed for O and H isotope compositions.

RESULTS

Mineralogy

All sinters display thin (mm scale) lamination and are mainly composed of opaline spicules (ranging up to 5 mm in length; Figure 3), which commonly incorporate detrital andesite grains. Highly disordered (poorly crystalline) opal-A is the dominant phase, as evidenced by the broad semi-coherent scatter peak at $\sim 26.3^\circ 2\theta$ $\text{CoK}\alpha$ ($\sim 4.0 \text{ \AA}$) in the XRD pattern (Figure 3). XRD analysis using the method of Herdianita et al. (2000a) show half maximum intensity values in the range of 7.4 to $7.9^\circ 2\theta$ (corrected to $\text{CuK}\alpha$), which is typical for recently modern formed sinters (Herdianita et al. 2000b). Maturation of opal-A to more ordered paracrystalline silica polymorphs (i.e., opal-C and opal-CT; Smith 1998; Lynne and Campbell 2004) was observed in sinters from Vent 2, however no systematic vertical or horizontal trend in paragenesis was observed amongst the specimens studied. WDS mapping of trace Al content shows the sinters have a spatial distribution corresponding to the laminations (Figure 4). XRD and thermogravimetric (data not shown) analyses do not indicate Al-bearing clay minerals as a source of the sinter Al laminations.

Differences noted between 2003 and 2004 samples prepared using the two protocols include a greater preservation of microbial mats attachment sites and EPS morphology in the 2004 samples. Bennett and Engell (2004) indicate that Cacodylate buffer does not react well with sulfate minerals, as they dissolve quickly in the fixative. Although evidence for trace amounts of sulfate minerals exist in the sinter, there were no noticeable effects on the 2004 samples.

Representative images of trace minerals found in the sinters are shown in Figure 5, including pyrite with octahedral and framboidal habits (Figure 5a–5c). Silica overgrowths commonly formed a drusy cover on pyrite surfaces (Figure 5a). Silica also partially covers pyrite surfaces as siliceous rods, which are interpreted to be encrusted microbes (Figure 5b). Framboids reside on top of the microbial mat and often appear to be encompassed by a thin coating of amorphous material too thin to identify with SEM-EDS (Figure 5c). Iron oxide/hydroxide occurs as crusts attached to filaments, which are believed to be extracellular polymeric substances (EPS) (Figure 5d). These microbial-iron-bearing mineral associations are common. The sinters occasionally feature an opal-A honeycomb texture composed of micron sized depressions (Figure 5e). Opal-A was typically noted as micron sized spheres with some instances of botryoidal clusters and smooth surfaces. Rare carbonate grains occur surrounded by organic material (Figure 5f). Table 2 lists minerals found in the sinter.

The rock-substrate of Vent 1 is highly altered andesite that is composed of clay minerals, whereas the rock substrate for Vent 2 is dominantly andesite that has been altered to opal-A

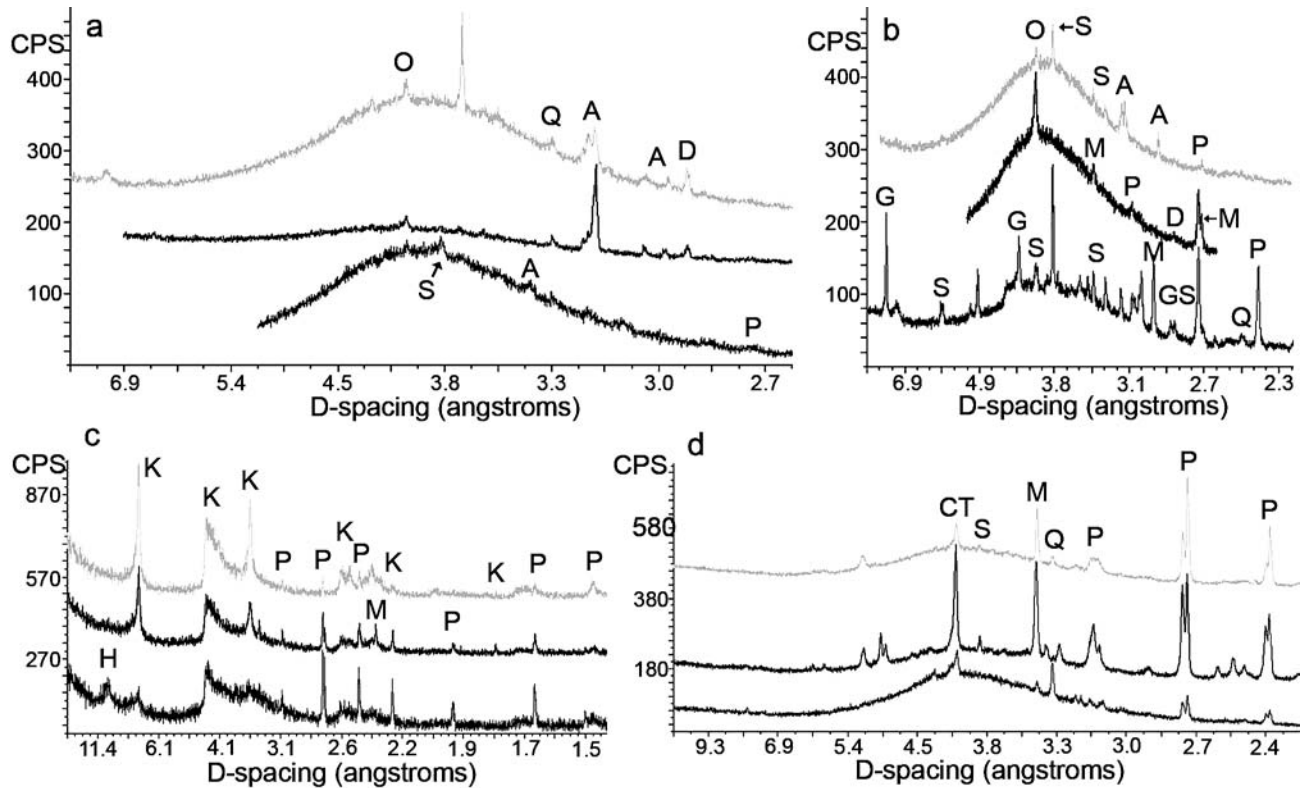


FIG. 3. Selected XRD patterns of siliceous sinters and substrate. Sintners from both springs, Vent 1 (a) and Vent 2 (b) are dominated by opal-A shown by the broad central peak. The diffractograms in (a) are arranged from top to bottom including samples JK03006, JK03-007, and JK03-008 as seen in Fig. 2a. Peaks are labeled as major reflections for the phases O = opal-A, A = andesine, Q = quartz, S = sulfur, D = dolomite, P = pyrite, G = gypsum, K = kaolin group, CT = opal-CT, and M = marcasite. The diffractograms in (b) are arranged from top to bottom including samples JK03-032a, JK03-032b, and JK03033 as seen in Fig. 2b. (c) The substrate in Vent 1 is dominated by kaolin group minerals, whereas the substrate for Vent 2 (d) is dominated by opal-A. The diffractograms in (c) represents same sample sequence as in (a) and in (d) represents same sample sequence as in (b). CPS = counts per second.

(Figure 3d). Vent 2 contains substrate with opal-CT/A (Lynne and Campbell 2004). Iron sulfides were found in both the sinter and substrate (Figure 3). Kaolin group minerals (Figure 6a) are the dominant clays, with some instances of halloysite tubular morphologies (Figure 6b–6d) observed in Vent 1. Pyrite, in

the form of cubes, framboids, and veins, is disseminated grains throughout the rock and most likely authigenic (Figure 6c). Lath-shaped barite (Figure 6e) and the occasional barite rose (Figure 6f) are also found throughout the rocks. Cinnabar is found as a vein running through the substrate (Figure 6g). The

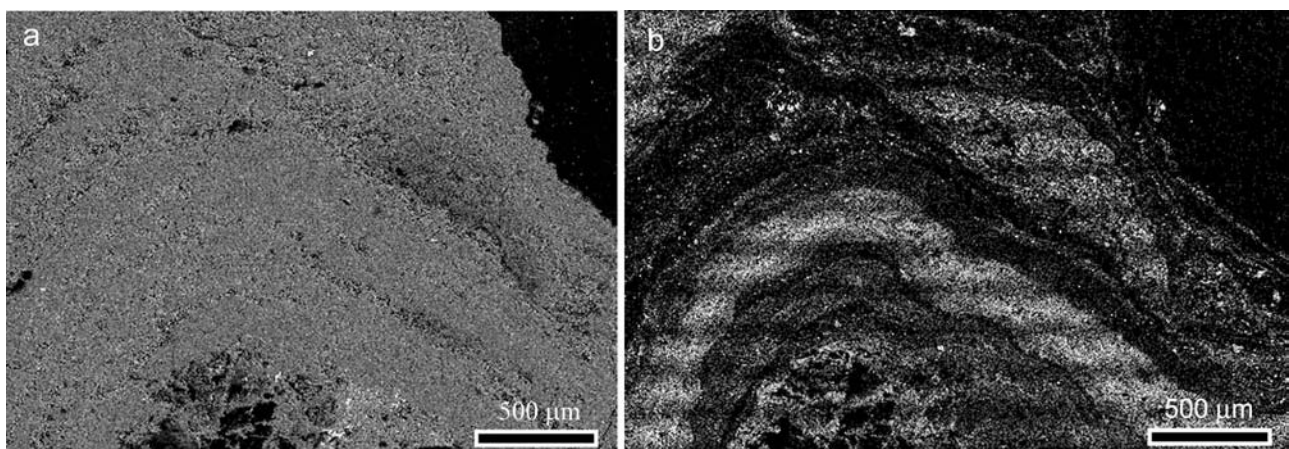


FIG. 4. (a) Secondary electron image and (b) wavelength dispersive spectroscopy trace aluminum mapping of sinter from JK03-007. XRD and thermogravimetric (data not shown) analyses do not indicate Al-bearing clay minerals as a source of the sinter Al laminations. This trace banding signature is likely something that would remain after long periods of geologic time and diagenesis.

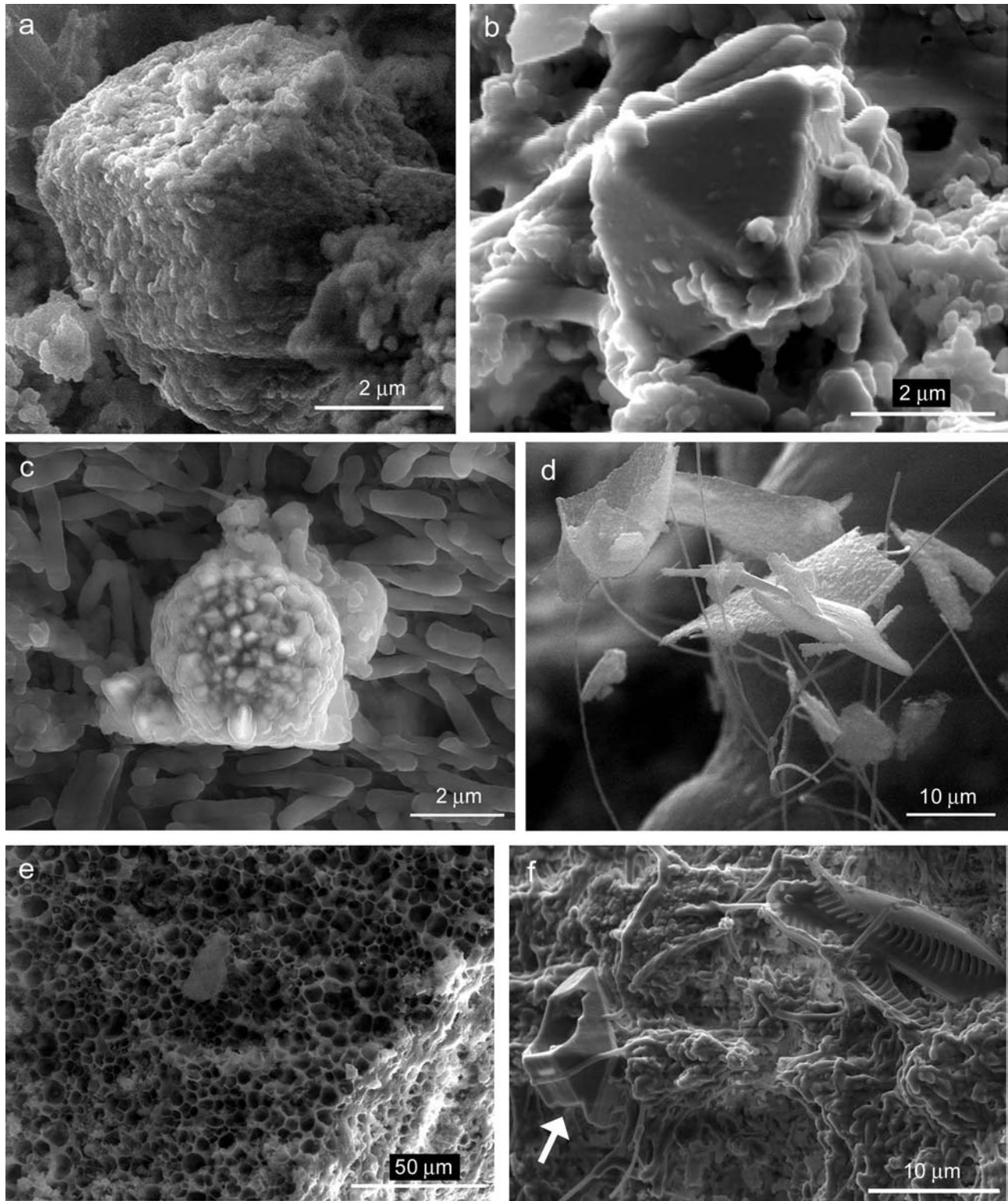


FIG. 5. Microbe-mineral habits of sinter from Vent 1 analyzed using SEM and EDS analysis. (a) Cubic shaped pyrite covered in silica, (b) octahedral pyrite surfaces with attached siliceous rods, (c) framboidal pyrite on a spicule tip in a microbial mat, (d) iron oxide/hydroxide crusts attached to extracellular polymeric substances (EPS), (e) honeycomb opal-A texture of sinter, and (f) carbonate (arrow) near a silicious diatom test and EPS.

TABLE 2
Mineralogy of sinters determined through XRD and EDS analysis

Mineral or phase	Formula	Vent 1	Vent 2
Opal-A ^{†*}	SiO ₂ ·nH ₂ O	X	X
Opal-CT*	SiO ₂ ·nH ₂ O	X	
Quartz*	SiO ₂	X	X
Calcite*	CaCO ₃	X	
Dolomite*	CaMg(CO ₃) ₂	X	X
Witherite [†]	BaCO ₃	X	X
Elemental sulfur*	S	X	X
Gypsum*	CaSO ₄ ·H ₂ O	X	
Barite [†]	BaSO ₄	X	X
Alunite*	KAl ₃ (SO ₄) ₂ (OH) ₆		X
Jarosite*	KFe ₃ (SO ₄) ₂ (OH) ₆		X
Pyrite ^{†*}	FeS ₂	X	X
Marcasite*	FeS ₂		X
Greigite*	Fe ₃ S ₄		X
Magnetite*	Fe ₃ O ₄		X
Hematite*	Fe ₂ O ₃		X
Manganese oxide [†]	MnO(OH)	X	
Titanium oxide [†]	TiO ₂	X	X
Cassiterite [†]	SnO ₂	X	
Ilmenite [†]	FeTiO ₃	X	
Chromite [†]	FeCrO ₄	X	
Gold [†]	Au	X	
Halite [†]	NaCl	X	
Sylvite [†]	KCl	X	
Kaolin group*	Al ₂ Si ₂ O ₅ (OH) ₄	X	
Andesine*	(Na,Ca)(Al,Si)AlSi ₂ O ₈	X	X
Pyroxene [†]	Fe-Al-silicate	X	

[†]Determined through EDS analysis.

*Determined through XRD analysis.

alunite group mineral minamiite occurs as isolated rod shaped clusters (Figure 6h). Jarosite (another alunite group mineral) is found at Vent 1. Table 3 lists additional mineral phases identified in the altered rock underneath the sinter using EDS and XRD.

Silicified tubes within sinters commonly form as a remnant of microbial cellular entombment resulting in an extracellular silica mold (Schultze-Lam et al. 1995; Cady and Farmer 1996; Jones and Renaut 1996; Renaut et al. 1998). Some of the silicified tubes found within Jenn's Pools are segmented (Figure 7a), while others are long and linear. All of the silicified tubes have rough exteriors and smooth interiors, and the degree of silica accumulation varied as some tubes are thickly mineralized (Figure 7a) while others are thin (Figure 7b).

Microbial Mat Mineralization

Microbial mat samples found attached to siliceous sinters are partially mineralized with colloidal opal-A (Figure 8). EDS and

TABLE 3
Mineralogy of rock substrate by XRD and EDS analysis

Mineral or phase	Formula	Vent 1	Vent 2
Opal-A ^{†*}	SiO ₂ ·nH ₂ O	X	X
Opal-CT*	SiO ₂ ·nH ₂ O		X
Quartz*	SiO ₂	X	
Calcium carbonate [†]	CaCO ₃		X
Witherite [†]	BaCO ₃	X	
Barite [†]	BaSO ₄	X	X
Jarosite*	KFe ₃ (SO ₄) ₂ (OH) ₆	X	
Minamiite [†]	(Na,Ca,K)Al ₃ (SO ₄) ₂ (OH) ₆		X
Gold [†]	Au		X
Pyrite ^{†*}	FeS ₂	X	X
Marcasite*	FeS ₂	X	X
Cinnabar [†]	HgS	X	
Magnetite*	Fe ₃ O ₄	X	
Titanium oxide [†]	TiO ₂	X	X
Ilmenite [†]	FeTiO ₃	X	
Kaolinite ^{†*}	Al ₂ Si ₂ O ₅ (OH) ₄	X	X
Halloysite [†]	Al ₂ Si ₂ O ₅ (OH) ₄ ·H ₂ O	X	

[†]Determined through EDS analysis.

*Determined through XRD analysis.

high-resolution TEM (HRTEM) analysis of the spheres revealed the spheres are composed of silica and oxygen with no crystal ordering. The mat surface from Vent 2 (JK04-019a) contains the most heavily mineralized cells with multiple layers of colloidal opal-A surrounding cells (Figure 8a–8c). Mineralization occurs away from the cell wall, which is possibly due to low density EPS not visible by TEM or an artifact due to shrinkage during sample preparation. Occasionally, the cell wall is thinly mineralized (Figure 8b). Hollow silicified structures are found with the shape and size of cells (Figure 8a, c). Further into the mat (JK04-019a) the silicified crusts became thinner, cells are less mineralized, and intracellular membranes are apparent (Figure 8d). Both mineralized and unmineralized cells are found residing within mineralized tubes (Figure 8e).

The mat sample collected adjacent and ~2 mm above (JK04-019b) in Vent 2 differed such that most all of the cells (~95%) contained intracellular membranes (Figure 8f). These membranes resemble thylakoids (photosynthetic membranes) found in photosynthetic microorganisms, such as cyanobacterium *Synechococcus lividus* (Edwards and Gantt 1971).

Cells are found sometimes clustered together and surrounded by lightly mineralized strands believed to be EPS (Figure 8g).

A Vent 2 mat sample from approximately 1 cm opposite the side of sinter JK04-019a (JK04-019c) contained abundant rod-shaped structures with a single strand running across the cell (Figure 8h). Cells in close proximity (microns) are in some cases lightly mineralized with silica and other not mineralized (Figure 8h). Mineralized cells here appear to represent the incipient

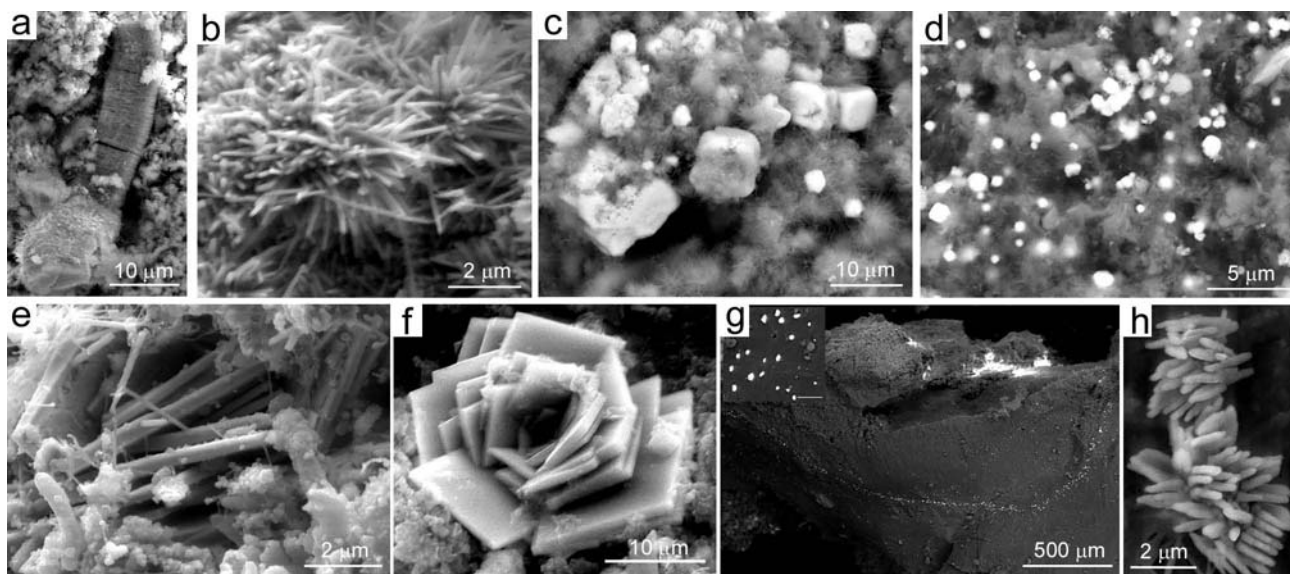


FIG. 6. Microbe-mineral habits of the rock substrate examined using SEM/EDS analysis. (a) Stacked vermiform kaolinite crystals, (b) halloysite tubes, (c) pyrite cubes surrounded by halloysite, (d) disseminated pyrite amongst halloysite, (e) barite laths, (f) barite rose, (g) cinnabar vein running through sample (inset higher magnification with scale bar = 20 μm), and (h) bladed to rod-shaped minamiite crystals.

stage of opal nucleation because the opal particles are smaller than those in the other mats, particularly when compared to particles located in cells mineralized both within and on the outside. Sectioning further into this mat revealed that the cells become more heavily silicified (Figure 8i).

Mat samples collected on the northeast side of Vent 2 (JK04-020) are unmineralized with only rare occurrences of mineralized tubes. Polyphosphate inclusions are noted (Figure 8j), and likely used as a phosphate reservoir and energy source for intracellular prokaryote metabolism. Many of the cells are segmented, some of which contained two or three concentric layers of intracellular membranes. The cells with intracellular membranes are morphologically different than the other Vent 2 samples (i.e., suggesting a different microbial species); however, they did not show a difference in the degree of mineralization. A mat sample from the northwest side of Vent 2 (JK03-036)

contains a few mineralized tubes with no evidence of internal structural preservation. These extracellular tubes are composed of nano-sized opal spheres that extended outward from the tubes in a radial fashion.

When comparing Vent 1 to Vent 2, the mats in the former are not as heavily mineralized. Unmineralized cells containing intracellular membranes occasionally occur in Vent 1. For example the mat from the southwest side of Vent 1 shows cells that are cocci, with some segmented and chains of cells (Figure 8k). The largest silicified cells are found on the southwest edge of Vent 1 (Figure 8l; JK03-037a). Most cells are greater than 2 microns in diameter and surrounded by a sheath. Strands extending from the surface of the cell, likely silicified EPS, are more thickly silicified than that occurring around the sheath. Most of the larger cells had one layer of mineralization around the cell, whereas the smaller cells typically did not.

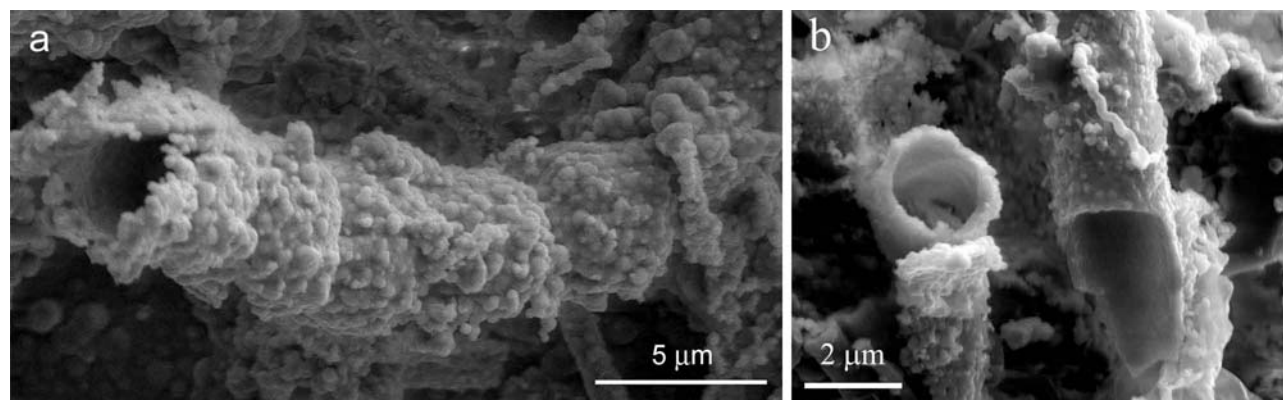


FIG. 7. Silicified tubes with smooth interiors and rough exteriors. (a) Segmented tube attached to the substrate and (b) broken thinly silicified tubes.

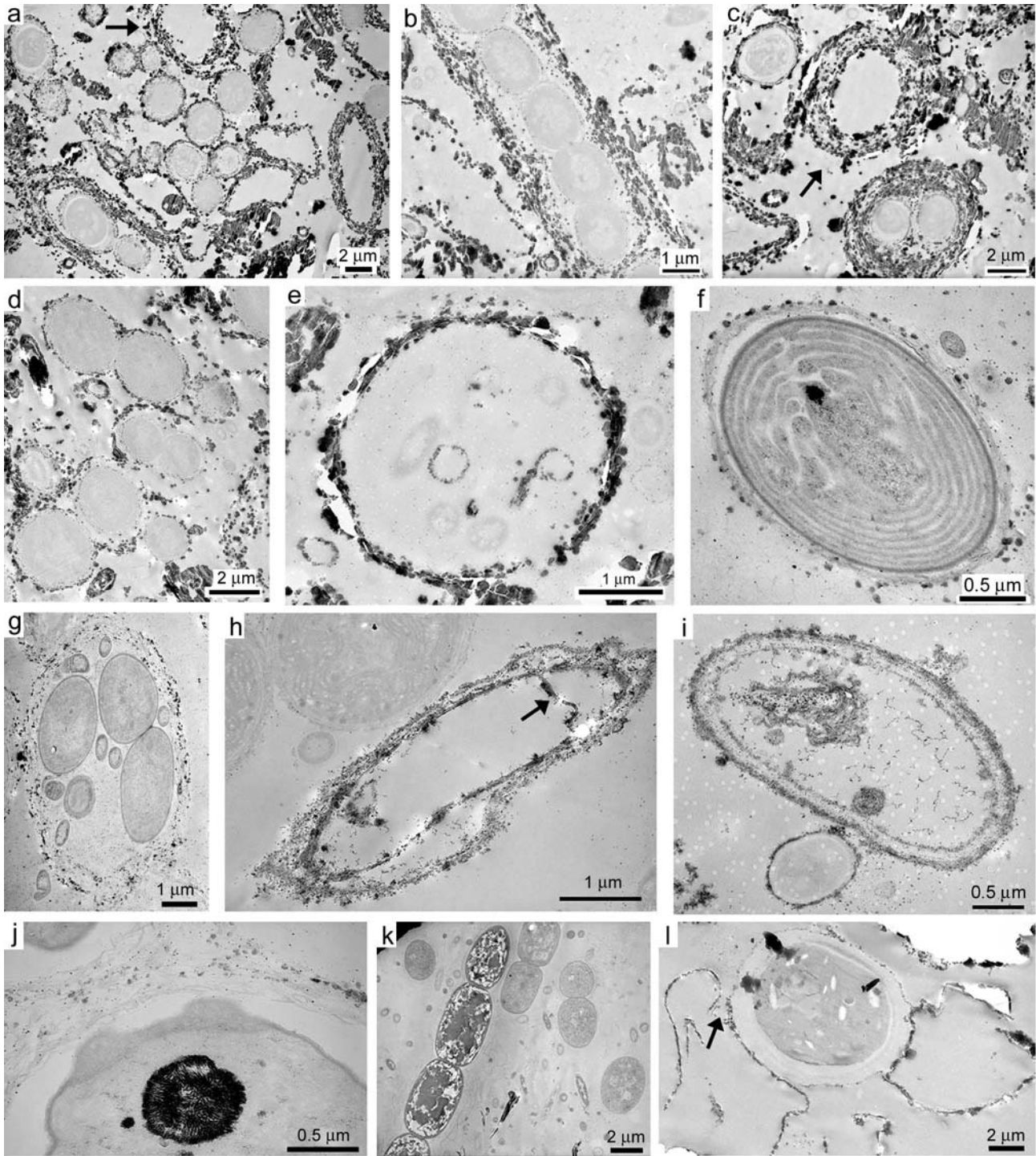


FIG. 8. Transmission electron micrographs of mat samples collected from sinter deposits at Vent 2 (a–j), and Vent 1 (k–l). (a) Extracellular silicification of cells and silicified molds (arrow; JK04-019a), (b) Silicified EPS surrounding cell and silicification of cell wall (JK04-019a), (c) heavily silicified cells and extracellular silicified mold (arrow; JK04-019a), (d) thinly mineralized cells with intracellular membranes (JK04-019a), (e) mineralized tubes with smaller mineralized and unmineralized cells within tube (JK04-019a) (f) intracellular membranes of lightly silicified cell (JK04-019b), (g) cells surrounded by lightly mineralized EPS (JK04019b1), (h) silica mineralized rod-shaped cell with internal segment (arrow) next to unmineralized cells in the upper left of the micrograph (JK04-019c), (i) silica on cell surface (JK04-019c), (j) polyphosphate granule within cell (dark granules; JK04-020), (k) unmineralized cells; smaller cells have intracellular membranes (JK04-024), (l) large cell with silica around cell and silicified strands extending from the cell some of which appear detached (arrow; JK03-037).

Bladed structures and their alteration products (Figure 9) are noted within the mats from Vent 1. The blade structures appear to be volcanic glass. The conchoidal fractures result from breaking during microtoming. HRTEM analysis shows they are composed of andesitic glass and lack crystal ordering. The glasses are often found altering into a kaolin group mineral (e.g., incipient stages in Figure 9a; later stage of alteration in Figure 9b).

DISCUSSION

Mineralogy

The sinters forming in Jenn's Pools are relatively young as they are dominated by opal-A. The maturation of opal-A to more ordered silica polymorphs (i.e., opal-CT, quartz) within the sinters was not noted, as evidenced by the crystallinity index of ~ 7.5 (Herdianita et al. 2000a). The only onset of opal-CT formation was noted within the substrate of one sample found at Vent 2. This lack of paragenetic transformation is likely due to the young age of the sinters but it also may be related to the presence of Al as a minor component of the sinters (see Figure 4). XRD and thermogravimetric analysis (data not shown) do not indicate the presence of clay minerals in the sinter. Only kaolin group minerals are found within the rock substrate of Vent 1. To date Al laminations within sinters have not been reported in the literature. Aluminum commonly substitutes for Si^{4+} in silica polymorphs (Railsback 2003). Al-rich laminae within the sinters may be related to a combination of high Al concentrations and fast rates of silica precipitation from solution. The local dissolution of volcanic glasses and andesine provide evidence for both a Si and Al source. Jones and Renaut (2004) have noted that in highly silica-saturated solutions, sinter laminae vary in the amount of water within the opal-A structure. When opal-A grows rapidly, water content of the sinters increases. The greater water content in the polymerized silica network increases the likelihood for disorder, which in turn increases the likelihood for trace levels of isomorphous Al substitution into the opal structure.

The difference in Vent 1 and Vent 2 sinter and substrate mineralogy is likely due to the chemistry and hydrology of the emerging spring fluids. The fluid chemistry and mineralogy (Tables 1, 2, and 3) of Vent 1 indicate a mildly acidic spring with relatively steady discharge. Vent 2 surges and is more of a mixed sulfate-chloride-bicarbonate. However, the extent to which microorganisms have on the formation of some of the minerals should be considered. Almost half of the mineral phases listed in tables 2 and 3 may form as a result of microbial metabolic processes and/or are commonly formed at the cell surface (mineral phases compared to those listed in Weiner and Dove 2003). The iron-bearing mineral phases found in the sinters are commonly associated with organics, which may provide metabolic redox benefits for the microorganisms (Kyle and Schroeder 2007).

The clay alteration of the rocks within Vent 1 results by acid hydrolysis of the original andesitic rock. In addition to abiotic alteration, kaolin group minerals within the green microbial mats

attached to the sinters (Figure 9) may have formed due to microbial metabolic processes that produce acid within the mats. Microbial activity has the potential to catalyze the transformation of volcanic glass to clay minerals (Tazaki 2005). The pH range of both vents is 5.3 to 5.9, at which rates of abiotic weathering of silicates is expected to be slow (Chou and Wollast 1985; Welch and Ullman 1993, 1996). Aluminosilicate dissolution kinetics can be increased by two orders of magnitude by bacterial production of organic and inorganic acids (Barker et al. 1997; Schwartzman and Volk 1989, 1991). Although most of the clay formation is dominantly due to sulfuric acid leaching and hydrothermal activity, clay formation may potentially be accelerated by microbial activity.

Microbial Mineralization

The dominant form of microbial mineralization noted thus far is silicification. TEM shows direct evidence of opal-A spheres surrounding microbial cells (Figure 8a–d, f, l), with the occasional instance of opal-A penetration of the outer cell wall (Figure 8b). Microbial silicification within this system is likely occurring passively as the cells becoming mineralized are in zones of higher evaporation rates (the air/water interface at the spring rim) and along the spring outflows (lower temperatures). Microbial cells and their products (EPS) act as templates for sinter formation (Cady and Farmer 1996) due to the low energy barrier towards nucleation. Extracellular bacterial silicification appears to occur via two mechanisms: (1) direct contact between the dissolved silica and the microbial cell wall (Mera and Beveridge 1993; Westall et al. 1995), and/or (2) the formation of a metal ion bridge between the cell wall and silica in solution (Mera and Beveridge 1993; Fortin and Beveridge 2000). The bacterial cell wall typically contains abundant functional groups (i.e., carboxyl and phosphoryl groups) that give the cell a net negative charge. Many of the cells undergoing silicification by opal-A have died and cellular material has since degraded, leaving extracellular silicified molds as the only evidence of microbial activity (Figures 7 and 8a,c). However, silicification of EPS does not always cause cell death (Phoenix et al. 2000). When mineralization is restricted to the EPS, bacterial cells can still be metabolically active. Detrimental effects to the cells viability begins when the cell wall becomes mineralized limiting nutrient intake and causing the buildup of metabolic by-products (Phoenix et al. 2000). When the EPS structure breaks down, smaller opal-A spheres and orthosilicic complexes may be able to pass through the EPS layer and nucleate upon the cell wall (Phoenix et al. 2000).

Cells that have undergone the greatest silicification are in alcoves near the vents. Vent 2 samples collected from the northwest side of the vent are affected by the surging of the spring. The most mineralized mats occur near the surge maximum (JK04-019). The fluids emerging from pools are locally undersaturated for opal-A precipitation (Table 1; Gunarsson and Arnórsson 2000). Mats facing the spring are the most silicified,

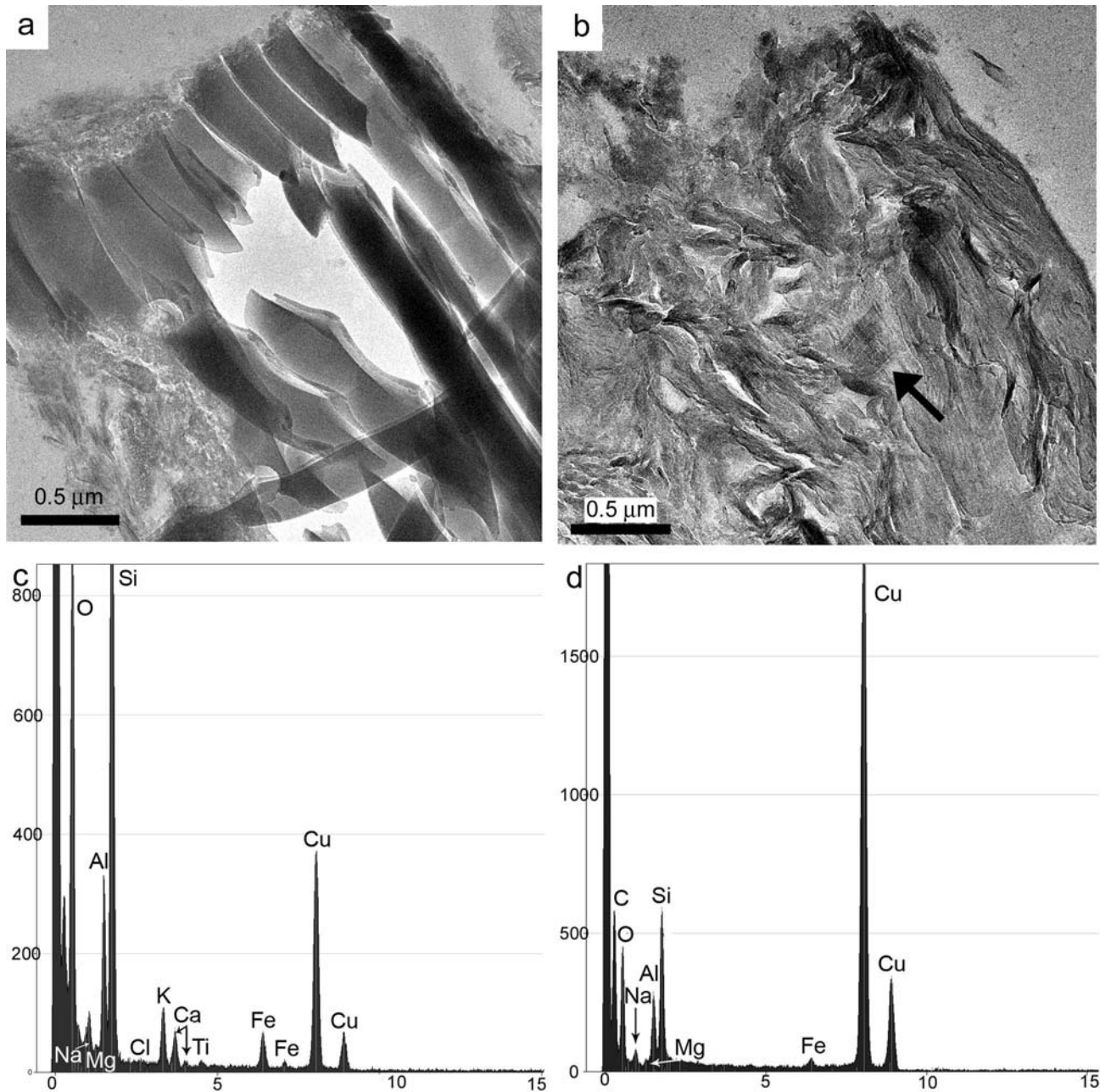


FIG. 9. (a) Volcanic glass and (b) kaolin group minerals found in JK04-024-b. The corresponding EDS spectra are similar to (c) felsic volcanic glass and (d) kaolinic clays (d). Vertical scale in count/sec/energy (keV). The volcanic glass is shown altering into clay in the lower left of the micrograph (a), and remnants of the glass are noted in the clay (arrow) (b). Cu signal is due to copper grid used to stabilize the sections in the microscope. Conchoidal fracturing of the glass is an artifact from microtoming with a diamond knife.

whereas on the opposite edge of the same sample, the mats are only lightly mineralized, perhaps reflecting difference in rates of evaporation or flushing by spring discharge. Another region that displays intense silicification is the northwest side of Vent 1. Although not thickly mineralized as Vent 2, the outer surface of cells become silicified, including EPS strands extending away from the cell (Figure 8I). Chan et al. (2004) deduced that polysaccharides excreted from the cell localize precipitation reactions

in which the mineralized polymer can be later detached from the cell. One implication of this study is that bacteria discard the mineralized strands to prevent cellular entombment. This mechanism may also apply to the silicified and the unattached EPS strands noted above. The EPS extending outward from the cell contained a majority of the silicification away from the cell surface, which in some instances appeared detached from the cell. The detached appearance could be an artifact due to a three

dimensional structure being viewed in 2 dimensions through the TEM, or a result of the fixation process causing detachment of the silicified strands.

Possible advantages of extracellular mineralization of opal-A include protection from physical damage (high intensity sunlight; Wyman and Fay 1986; Phoenix et al. 2006) and predation (Brown and Wolfe 2006; Phoenix et al. 2000). Silicification may act as an antidesiccant if the silica is precipitated in a hydrated state (Phoenix et al. 2000). In this study, silicified tubes are found to contain smaller microorganisms (Figure 8e). We suggest the silicified tubes may also provide protection as they prevent direct exposure to physical damage (i.e. ultraviolet radiation) and predation by other microorganisms.

Preservation Potential of Microbial Activity

If the morphological and mineralogical biosignatures found within modern terrestrial hot spring system at Jenn's Pools are diagnostic features, then the question remains as whether or not these features would be found in the geologic record? Toporski et al. (2002) suggested that in a closed system, temperature and pressure do not increase, silicified microbes are unlikely to undergo *in situ* dissolution/precipitation reactions. This would enable the silicified microfossils to become preserved for longer periods of time. Within our study, the silicified microbes within the mats are far more abundant than the extracellular silicified molds found within the sinters of Jenn's Pools suggesting silicified microbes within the mats are infrequently preserved within the sinter. Time is also an important factor in silica polymorph dissolution/precipitation reactions (Fournier 1985). The dissolution/precipitation reaction of opal-A to opal-CT can occur over thousands of years, which may destroy extracellular silicified molds as opal-A dissolves back into solution. Herdianita et al. (2000) showed the mineralogy and textures of modern to Miocene age sinters change through time as opal-CT and quartz formed from opal-A and fossilized microbial filaments are modified or destroyed. The interior silicified mold diameter (used to determine original diameter of microbial cells) also becomes smaller as silica infills the tubes during opal-A maturation to opal-CT (Lynne and Campbell 2003). Lynne and Campbell (2003) found that this silica sinter maturation causes fine details of silicified molds to be lost. Recent studies, however, suggest a chemical signature may be preserved within sinters, as modern siliceous sinters from New Zealand have been shown to preserve lipid material (Pancost et al. 2005, 2006).

CONCLUSIONS

When determining the growth and relative age of sinter deposits, trace element content and abundance should be considered. All laminations noted within Vent 1 deposits indicate zones of rapid precipitation, and may potentially interrupt the opal-A to opal-CT transformation resulting in a younger age for sinter deposits. A benefit of decreasing opal paragenetic transformations is extending the existence of microbial morphotypes, such as the silicified tubes. Extracellular silicification was the most

common form of mineralization noted, as it was the most common inorganic phase to interact with microbial cells and/or EPS. An advantage of remnant microbial tubes is that they may act as a protective containment (niche) to microorganisms that reside within the tubes. In the recent geologic record (rocks few thousands of years old) the tubular structures will likely be recognized as microbial remnants. Although these structures will unlikely be preserved in the long term geologic record (few million of years) as opal-A dissolves back into solution altering and/or destroying most of the silicified molds. As microbial morphological preservation decreases throughout time, one of the remaining markers of biological activity will be in the associated mineral assemblage. Minerals that are typically associated within forming in hydrothermal environments, may also be formed as a result of microbial activity. One example of this case in Jenn's Pools is in the microbial contribution to clay mineral formation.

Future work on these samples to better characterize their preservation potential would be to conduct stable isotope and lipid analysis to reveal the isotopic and biomarker signatures, respectively. Laboratory analysis on the effects opal-A dissolution and opal-CT precipitation on extracellular silicified molds would offer further insight into the destruction or possible preservation of these microbial signatures.

ACKNOWLEDGMENTS

We thank Doug Crowe, Chris Romanek, Andy Neal, and Sherry Cady for their comments. John Shield and Don Roberts assisted with SEM analysis. We would again like to thank Doug Crowe and Gennadii Karpov for permission to use their map in Figure 1. This work was funded by a grant from the National Science Foundation Microbial Observatory Program (NSF MO 0238407) and the University of Georgia, Department of Geology Wheeler-Watts Fund. We thank Kronostky Preserve for permission to work in the Uzon Caldera.

REFERENCES

- Altermann W. 2001. The oldest fossils of Africa- a brief reappraisal of reports from Archean. *African Earth Sciences* 33:427-436.
- Barker WW, Welch SA, Banfield JF. 1997. Biogeochemical weathering of silicates minerals. In: Banfield JF, Nealson KH, editors. *Geomicrobiology: Interactions between microbes and mineral*. Washington, DC: Mineralogical Society of America. P 391-428.
- Bennett PC, Engel AS, Roberts JA. 2006. Counting and imaging bacteria on mineral surfaces: In: Patricia J, Maurice A, Lesley A, editors. *Methods of Investigating Microbial-Mineral Interactions*, CMS Workshop Lectures. Chantilly, VA: The Clay Mineral Society. P 37-78.
- Bonch-Osmolovskaya EA, Miroshnichenko ML, Slobodkin AL, Sokolova TG, Karpov GA, Kostrikina NA, Zavarzina DG, Prokof'eva MI, Rusanov II, Rimenov NV. 1999. Biodiversity of anaerobic lithotrophic prokaryotes in terrestrial hot springs of Kamchatka. *Microbiology* 3:398-406.
- Braunstein D, Lowe DR. 2001. Relationship between spring and geyser activity and the deposition and morphology of high temperature (>73°C) siliceous sinter, Yellowstone National Park, Wyoming. *J Sediment Res* 71:747-763.
- Brown PB, Wolfe GV. 2006. Protist genetic diversity in the acidic hydrothermal environments of Lassen Volcanic National Park, USA. *J Eukar Microbiol* 53:420-431.

- Cady SL, Farmer JD. 1996. Fossilization processes in siliceous thermal springs: trends in preservation along thermal gradients. In: Evolution of hydrothermal ecosystems of Earth (and Mars?) Wiley, Chichester (Ciba Foundation Symposium 202) P 150–173.
- Chan CS, De Stasio G, Welch AA, Girasol M, Frazer BH, Nesterova MV, Fakra S, Banfield JF. 2004. Microbial polysaccharides template assembly of nanocrystalline fibers. *Science* 303:1656–1658.
- Chou L, Wollast R. 1985. Steady-state kinetics and dissolution of albite. *Amer J Sci* 285:963–993.
- Edwards MR, Gantt E. 1971. Phycobilisomes of the thermophilic blue-green alga *Synechococcus lividus*. *J Cell Biol* 50:896–900.
- Ferris FG, Fyfe WS, Beveridge TJ. 1988. Metallic ion binding by *Bacillus subtilis*: Implications for the fossilization of microorganisms. *Geology* 16:149–152.
- Fortin D, Beveridge TJ. 2000. Mechanistic routes towards biomineral surface development. In: Baeuerlein E, editor. *Biomineralization: From Biology to Biotechnology and Medical Application*. Weinheim, Germany: John Wiley and Sons. P 7–24.
- Fournier RO. 1985. The behavior of silica in hydrothermal solutions. Review in *Economic Geology* 2:45–61.
- Gunnarsson I, Arnórsson S. 2000. Amorphous silica solubility and the thermodynamic properties of $\text{H}_4\text{SiO}_4^\circ$ in the range of 0° to 350°C at Psat. *Geochim Cosmochim Acta* 64:2295–2307.
- Herdianita NR, Browne PL, Rodgers KA, Campbell KA. 2000a. Mineralogical and textural changes accompanying ageing of silica sinter. *Mineralium Deposita* 35:48–62.
- Herdianita NR, Rodgers KA, Browne PRL. 2000b. Routine instrumental procedures to characterize the mineralogy of modern and ancient silica sinters. *Geothermics* 29:65–81.
- Hurst VJ, Schroeder PA, Styron RW. 1997. Accurate quantification of quartz and other phases by powder X-ray diffractometry. *Anal Chim Acta* 337:233–252.
- Jones B, Renaut RW. 1996. Influence of thermophilic bacteria on calcite and silica precipitation in hot springs with water temperatures above 90°C: evidence from Kenya and New Zealand. *Can J Earth Sci* 33:72–83.
- Jones B, Renaut RW. 2004. Water content of opal-A: implications for the origin of laminae in geysers and sinter. *J Sediment Res* 74:117–128.
- Karpov GA. 1995. WRI-8 Post Session Field Trip to Kamchatka Part II: Uzon-Geysir Depression. Proceedings of the 8th international symposium on water-rock interaction (WRI-8), Vladivostok, Russia 31–33.
- Karpov GS, Naboko SI. 1990. Metal contents of recent thermal waters, mineral precipitates and hydrothermal alteration in active geothermal fields, Kamchatka. *J Geochem Explor* 36:57–71.
- Knoll A. 2003. *Life on a Young Planet: The First Three Billion Years of Evolution on Earth*. Princeton, New Jersey: Princeton University Press.
- Konhauser KO, Jones B, Reysenbach A, Renaut RW. 2003. Hot spring sinters: keys to understanding Earth's earliest life forms. *Can J Earth Sci* 40:1713–1724.
- Konhauser KO, Phoenix VR, Bottrell SH, Adams DG, Head IM. 2001. Microbial-silica interactions in Icelandic hot spring sinter: possible analogues for some Precambrian siliceous stromatolites. *Sedimentology* 48:415–433.
- Konhauser KO, Jones B, Phoenix VR, Ferris G, Renaut RW. 2004. The microbial role in hot spring silicification. *Ambio* 33:552–558.
- Kyle JE, Schroeder PA. 2007. Role of smectite in siliceous sinter formation and microbial texture preservation: Octopus Spring, Yellowstone National Park, Wyoming, USA. *Clays Clay Minerals* 55(2):189–199.
- Lalond SV, Konhauser KO, Reysenbach AL, Ferris FG. 2005. The experimental silicification of *Aquificales* and their role in hot spring sinter formation. *Geobiology* 3:41–52.
- Lynne BY, Campbell CA. 2003. Diagenetic transformations (opal-A to quartz) of low- and mid-temperature microbial textures in siliceous hot-spring deposits, Taupo Volcanic Zone, New Zealand. *Can J Earth Sci* 40:1679–1696.
- Lynne BY, Campbell KA. 2004. Morphologic and mineralogic transitions from opal-A to opal-CT in low-temperature siliceous sinter diagenesis, Taupo Volcanic Zone, New Zealand. *J Sediment Res* 74:561–579.
- McKay DS, Gibson EK, Thomas-Keprta KL, Vali H, Romanek CS, Clemett SJ, Chillier X, Maechling CR, Zare RN. 1996. Search for Past Life on Mars: Possible Relic Biogenic Activity in Martian Meteorite ALH84001. *Science* 273:924–930.
- Mera MU, Beveridge TJ. 1993. Mechanism of silicate binding to the bacterial cell wall in *Bacillus subtilis*. *J Bacteriol* 175:1936–1945.
- Mountain BW, Benning LG, Boerema JA. 2003. Experimental studies on New Zealand hot spring sinters: rates of growth and textural development. *Can J Earth Sci* 40:1643–1667.
- Pancost RD, Pressley S, Coleman JM, Benning LG, Mountain BW. 2005. Lipid biomolecules in silica sinters: indicators of microbial biodiversity. *Environ Microbiol* 7:66–77.
- Pancost RD, Pressley S, Coleman JM, Talbot HM, Kelly SP, Farrimond PF, Schouten S, Benning LG, Mountain BW. 2006. Composition and implications of diverse lipids in New Zealand Geothermal sinters. *Geobiology* 4:71–92.
- Phoenix VR, Adams DG, Konhauser KO. 2000. Cyanobacterial viability during hydrothermal biomineralization. *Chem Geol* 169:329–338.
- Phoenix VR, Bennett PC, Engel AS, Tyler SW, Ferris FG. 2006. Chilean high-altitude hot-spring sinters: a model system for UV screening mechanisms by early Precambrian cyanobacteria. *Geobiology* 4:15–28.
- Prokofeva MI, Kublanov IV, Nercessian O, Tourova TP, Kolganova TV, Bonch-Osmolovskaya EA, Spring S, Jeanthon C. 2005. Cultivated anaerobic acidophilic/acidotolerant thermophiles from terrestrial and deep-sea habitats. *Extremophiles* 9: 437–448.
- Renaut RW, Jones B, Tiercelin JJ. 1998. Rapid in situ silicification of microbes at Loburu hot springs, Lake Bogoria, Kenya Rift Valley. *Sedimentology* 45:1083–1103.
- Railsback BL. 2003. An earth scientist's periodic table of the elements and their ions *Geology* 31:737–740.
- Rodgers KA, Browne PRL, Buddle TF, Cook KL, Greatrex RA, Hampton WA, Herdianita NR, Holland GR, Lynne BY, Martin R, Newton Z, Pastars D, Sannazarro KL, Teece CIA. 2004. Silica phases in sinters and residues from geothermal fields of New Zealand. *Earth-Sci Rev* 66:1–61.
- Romanek CS, Grady MM, Wright IP, Mittlefehldt DW, Socki RA, Pillinger CT, Gibson EK. 1994. Record of fluid-rock interactions of Mars from the meteorite ALH84001. *Nature* 372:655–657.
- Rosing MT. 1999. ^{13}C -Depleted Carbon Microparticles in > 3700-Ma Seafloor Sedimentary Rocks from West Greenland. *Science* 283:674–676.
- Russell S, Hartmann L, Cuzzi J, Krot A, Gounelle M, Weidenschilling S. 2005. In: Lauretta D, Leshin LA, McSween HY, editors. *Meteorites and the early solar system II*. Tucson: University Arizona Press.
- Schopf JW, Kudryartsev AB, Agresti DJ, Wdowiak TJ, Czaja AD. 2002. Laser-raman imagery of Earth's earliest fossils. *Nature* 416:73–76.
- Schultze-Lam S, Ferris FG, Konhauser KO, Wiese RG. 1995. In situ silicification of an Icelandic hot spring microbial mat: implications for microfossil formation. *Can J Earth Sci* 32:2021–2026.
- Schwartzman DW, Volk T. 1989. Biotic enhancement of weathering and the habitability of Earth. *Nature* 340:457–459.
- Schwartzman DW, Volk T. 1991. Biotic enhancement of weathering and surface temperatures on Earth since the origin of life. *Paleogeogr Paleoclim Paleocool* 90:357–371.
- Smith DK. 1998. Opal, cristobalite, and tridymite: Noncrystallinity versus crystallinity, nomenclature of the silica minerals and bibliography. *Powder Diffract* 13:2–19.
- Slepova TV, Sokolova TG, Lysenko AM, Tourova TP, Kolganova TV, Kamzolnikina OV, Karpov GA, Bonch-Osmolovskaya EA. 2006. Carboxydocella sporoproducens sp. nov., a novel anaerobic CO-utilizing/H₂-producing thermophilic bacterium from a Kamchatka hot spring. *Int. J. Syst. Evol. Microbiol* 56:797–800.
- Tanner SD, Baranov VI, Bandura DR. 2002. Reaction cells and collision cells for ICP-MS: A tutorial review, *Spectrochim Acta Pt B: Atom Spectrosc* 57:1361–1452.

- Tazaki K. 2005. Microbial formation of a halloysite-like mineral. *Clays Clay Miner* 53:224–233.
- Toporski J, Steele A, Westall F, Thomas-Keprta K, McKay D. 2002. The simulated silicification of bacteria- New clues to the modes and timing of bacterial preservation and implications for the search for extraterrestrial microfossils. *Astrobiology* 2:1–26.
- Walsh MM. 1992. Microfossils and possible microfossils from the Early Archean Onverwacht Group, Barberton Mountain Land, South Africa. *Precamb Res* 54:271–292.
- Walsh MM, Lowe DR. 1985. Filamentous microfossils from the 3500 Myr-old Onverwacht Group, Barberton Mountain Land, South Africa. *Nature* 314:530–532.
- Weiner S, Dove PM. 2003. An overview of biomineralization processes and the problems of the vital effect. In: Dove PM, De Yoreo JJ, Weiner S, editors. *Biomineralization*. Washington, DC: Mineralogical Society of America. P 1–24.
- Welch SA, Ullman WJ. 1993. The effect of organic acids on plagioclase dissolution rates and stoichiometry. *Geochim Cosmochim Acta* 57:2725–2736.
- Welch SA, Ullman WJ. 1996. Feldspar dissolution in acidic and organic solutions. *Geochim Cosmochim Acta* 60:2939–2949.
- Westall F, Boni L, Guerzoni E. 1995. The experimental silicification of microorganisms. *Palaeontology* 38:495–528.
- Westall F, de Wit J, Dann J, van der Gaast S, de Ronde C, Gerneke D. 2001. Early Archean fossil bacteria and biofilms in hydrothermally-influenced sediments from the Barberton greenstone belt, South Africa. *Precamb Res* 106:93–116.
- Wyman M, Fay P. 1986. Underwater light climate and the growth of pigmentation of planktonic blue-green algae (Cyanobacteria): I. The influence of light quantity. *Proc Roy Soc Lond* 227:367–380.
- Zhang CL, Pearson A, Li YL, Mills G, Wiegel J. 2006. A thermophilic temperature optimum for crenarchaeol and its implication for archaeal evolution. *Appl. Environ. Microbiol.* 72:4419–4422.
- Zhao W, Weber C, Zhang CL, Romanek CS, King GM, Mills G, Sokolova T, Wiegel J. 2006. *Thermalkalibacillus uzonensis*, gen. nov. sp. nov., a novel alkalitolerant aerobic thermophilic bacterium isolated from a hot spring in Uzon Caldera, Kamchatka. *Extremophiles* 10:337–345.